Identifying deformation mechanisms in molecular dynamics simulations of laser shocked matter

T. G. White[a,b], A. Tikku[b], M. A. Silva[b], G. Gregori[a], A. Higginbotham[c], D. E. Eakins[b]

[a] *Department of Physics, University of Oxford, Parks Road, Oxford, OX1 3PU, United Kingdom*
[b] *Institute of Shock Physics, Imperial College London, London, SW7 2AZ, United Kingdom*
[c] *York Plasma Institute, University of York, York, YO10 5DD, United Kingdom*

Abstract

In this paper we demonstrate a new post-processing technique that allows straightforward identification of deformation mechanisms in molecular dynamics simulations. We utilise reciprocal space methods by calculating a per-atom structure factor (PASF) to visualise changes in volume, orientation and structure, thus allowing unambiguous discrimination between key deformation/relaxation mechanisms such as uniaxial strain, twinning and structural phase transformations. The full 3-D PASF is reduced to a 2-D representation by taking only those points which lie on the surface of an ellipsoid passing through the nearest reciprocal lattice points. Projecting this 2-D representation onto the set of spherical harmonics allows for a numerical characterisation of the system state that easily captures various plastic deformation mechanisms that have been historically difficult to identify. The technique is used to successfully classify high temperature twinning rotations in shock compressed tantalum and to identify the α to ω phase transition in group-IV hcp metals.

Keywords: Structure Identification, Shock waves, Molecular Dynamics, Twinning,, Plasticity

1. Introduction

Atomistic simulation through molecular dynamics (MD) has become an invaluable tool for modelling the response of material undergoing high rate

deformation, such as that experienced during material irradiation with a high intensity optical laser[1, 2]. Such conditions are of fundamental scientific interest and remain an active area of research due to their application in planetary science[3], materials synthesis[4] and within thermonuclear fusion research and the long-term goal of facilities such as the National Ignition Facility, USA[5, 6]. The short timescales and high strain-rates present in these experiments make them particularly amenable to MD simulation, which have become an indispensable tool for investigating the richness of lattice level behaviours activated at these high temperature and pressure conditions, such as defect generation, twinning, dislocation motion and structural phase transitions[7, 8, 9, 10].

Experiments in this field, routinely performed on state-of-the-art 4th generation light sources where the X-ray source is used as a probe, drive micron sized volumes of material to mega-bar conditions over picosecond timescales[11, 12, 13] and we are fast approaching a point where MD and free electron lasers (FELs) operate at commensurate scales. A recent experiment recorded in situ X-ray diffraction from Cu shocked to pressures of 100 GPa and demonstrated a remarkable agreement between MD and experiment, providing greater mechanistic understanding of the deformation mechanics present[11]. However, the analysis of large-scale MD simulations is non-trivial and real space methods currently have difficulty identifying some specific transitions of fundamental interest (α to ω phase transition, high temperature twinning, etc).

Classical MD simulations typically keep track of just particle positions and velocities which then evolve according to a Hamiltonian and a prescribed interatomic potential. Hence, characteristic features of plastic deformation such as slip planes, Burgers vectors, lattice rotations, phase transformations or even unit cells must be computed *a posteriori*. Numerous real-space order parameters exist such as coordination number, common neighbor analysis[14] (CNA), centrosymmetry parameter[15] or bond angle analysis[16] which excel at determining structural changes such as solid-solid phase transitions and gives excellent spatial resolution, allowing parameters to be calculated on a per-atom basis. However, they work only for common structures and the inherently real space nature of these techniques mean their accuracy remains extremely sensitive to local disorder from high temperatures or large defect generation, both of which are present in laser shocked matter. A summary of existing analysis techniques can be found in the review article by A. Stukowski[17].

Here we introduce a framework based on the per-atom structure factor (PASF) concept developed by Higginbotham *et al.*[18]. This reciprocal space technique is easily able to identify lattice level changes such as uniaxial compression, crystallographic orientation or phase transformations in highly disordered or high temperature samples. This extension, achieved through projecting an ellipsoidal slice of reciprocal space onto the set of spherical harmonics, produces a numerical characterization of the system that can be used to color or categorize the atoms to aid visualization, removing the need to know structures, strains or orientations *a-priori*.

The use of spherical harmonics in atomic structure identification is not new - see for example [19, 20, 21], or the section on Fourier descriptors in the work by Keys *e*t al. [22], which matches Harmonic decompositions of real space density. The plethora of techniques available highlight the difficulties associated with accurate structure identification. Used in conjunction with the per-atom structure factor Harmonic decomposition provides benefits in the analysis of laser-shocked solids that has not been presented before. In contrast to previous work our method remains intentionally sensitive to lattice compression, achieved through taking a slice rather than a projection of reciprocal space, and to lattice rotations, allowing identification of twinning and twin fraction. This work provides a middle ground which alleviates issues with existing approaches; this is demonstrated in the much more complex environment of a shock, where effects due to disorder must be mitigated.

2. Per Atom Structure Factor

The basis of this method is calculating the atomic structure factor, a technique analogous to taking the discrete Fourier transform of the atomic positions. The structure factor easily identifies periodicity in the crystal micro-structure and, in a solid with a single atomic species, is defined by,

$$S(\mathbf{k}) = \frac{1}{N}\left|\sum_{n=1}^{N} e^{i\mathbf{k}\cdot\mathbf{r_n}}\right|^2 \tag{1}$$

where $\mathbf{k}$ is a reciprocal space lattice vector and $\mathbf{r_n}$ are the atomic coordinates. The summation in equation 1 typically runs from $n = 1$ to N, where N is the total number of atoms in the simulation, hence the structure factor is by definition a non-local metric. For decades, calculation of the crystal

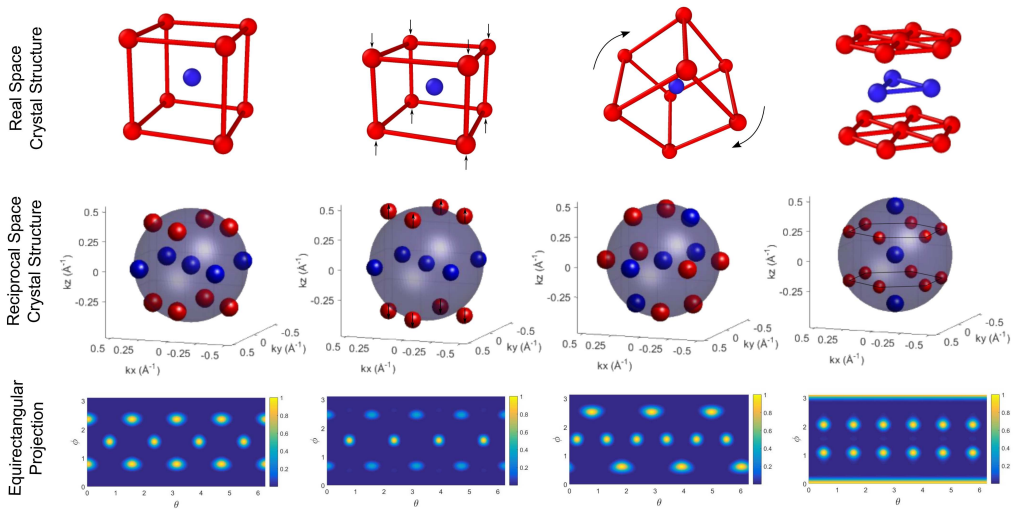

Figure 1: Prototypical evolution of the lattice-level micro-structure for a bcc system during a laser induced shock. From left-to-right is the unit cell, the effect of 20% uniaxial compression along z, a lattice rotation consistent with the $\{112\}<111>$ twin systems expected in bcc material and lastly a phase change to a hcp structure. Shown is the crystallographic unit cell (a), the iso-surface of the 3-D PASF (b) and the equirectangular projection of the ellipsoid slice (c). The color in the 3-D PASF is used to highlight the symmetries present.

structure factor has allowed comparison between experimentally recorded X-ray diffraction patterns and theoretically derived crystal micro-structures as, within the kinematic approximation, the intensity of an X-ray diffraction pattern is related to the modulus squared of the structure factor calculated over the X-ray interaction region[23].

In order to reduce the crystal structure factor to a per-atom quantity we reduce the region over which the summation in equation 1 runs to include only those atoms that lie within a predetermined radius around each target atom. This quantity we call the per-atom structure factor. A judicial choice of this radius is required, as too small a number will result in too few atoms being within the calculation sphere increasing the effect of noise and hiding any periodicity or symmetries present in the crystal. On the other hand, a larger radius will afford an increased reciprocal space resolution at the cost of real space resolution and thus could obscure features smaller than the chosen radius. Previous work has found a radius of 4 Å, typically producing a sphere containing between 10 and 20 atoms, to provide a good balance between these competing effects and has been used throughout this work[18].

An outline of the general method is given in Fig. 1. The top row shows real space representation of a body-centred cubic (bcc) crystal structure along with three additional structures that could occur during prototypical high rate crystal deformation; these are a 20% uniaxial compression along z, a lattice rotation consistent with the {112}<111> twin systems expected in bcc material and lastly a phase transformation into hexagonal close packed (hcp), e.g. the α to ϵ phase transition in iron. The middle row of Fig. 1 shows high resolution iso-surfaces of the PASF for each real space lattice, calculated with a reciprocal space resolution of 10^{-2} Å^{-1} and containing 10^6 k-points. From each 3-D PASF the deformation mechanism is readily apparent, as indicated by the arrows. However, there is a large computational cost with calculating such a number of reciprocal space values.

To reduce this computation cost without assuming *a-priori* knowledge of the system, here we instead calculate the value of the 3-D PASF on a ellipsoid slice through reciprocal space which passes through the nearest neighbour reciprocal lattice points, i.e. the outer vertices of the second Brillouin zone. The same reciprocal space resolution can be achieved with just 10^3 k-points. The final row of Fig. 1 shows the equirectangular projections, $S(\theta, \phi)$, of these ellipsoidal slices for each of the cases discussed above. In each case the effect of crystal deformation is easily identified by the 2-D plot and the crystal symmetries readily apparent; uniaxial strain leads to the k-space reflections

moving away from the origin reducing their intensity, a rotation causes the reflections to move on the surface but the number remain the same, while a phase transformation changes the pattern drastically. Although some information is lost from the 3-D to 2-D representation the huge computational speed up allows this per-atom quantity to be calculated for millions of atoms within minutes.

Previous work has taken linear slices through reciprocal space in order to visualise changes in the PASF, but has required *a-priori* knowledge of the deformation mechanism to determine where to slice the data; our method is more general and more lenient. However, the lengths of the three semi-principal axes of the ellipsoid must still be defined in advance; these should be chosen to intersect as many of the reciprocal space reflections as possible and intersect the outer vertices of the second Brillouin zone. For an initial bcc structure this is given by $a_\mathrm{k} = b_\mathrm{k} = c_\mathrm{k} = 2\pi\frac{\sqrt{2}}{a}$, for fcc it is given by $a_\mathrm{k} = b_\mathrm{k} = c_\mathrm{k} = 2\pi\frac{\sqrt{3}}{a}$ and for hcp it is given by $a_\mathrm{k} = b_\mathrm{k} = 2\pi\frac{4}{3a}$ and $c_\mathrm{k} = 2\pi\frac{2}{c}$. In each case a and c are the lengths of the unit cell in real space and a_k, b_k, c_k the lengths of semi-principal axes in reciprocal space. The inclusion of the factor of 2π is related to the definition of the reciprocal lattice.

It should be noted that although the ellipse is defined in terms of the initial lattice parameters it is generally not necessary to dynamically alter the ellipsoid during deformation. This is in part due to the broadening of the peaks in reciprocal space which is inversely proportional to the radius of the real space sphere over which the PASF is calculated. Since here the real space radius is extremely small, 4 Å in this case, reciprocal space blurring ensures even large deformations of up to 20% can be identified on the ellipsoid, see Fig. 1. Although allowing the ellipse to dynamically deform per atom could allow easier identification of crystal structure, removing any dependence on compression or rotation, it would introduce difficulties regarding correspondence between different atoms and increase computational requirements. Future work could extend the method introduced here in this way to further increase the generality of the method.

2.1. Projection onto Spherical Harmonics

Taking only an ellipsoidal slice of reciprocal space affords a computational speed up over calculating the full 3-D PASF. Furthermore, by projecting the 2-D PASF onto the set of spherical harmonics, defined as the angular portion of the solution to Laplace's equation, produces a series of coefficients characterizing the lattice deformation. The set of spherical harmonics form

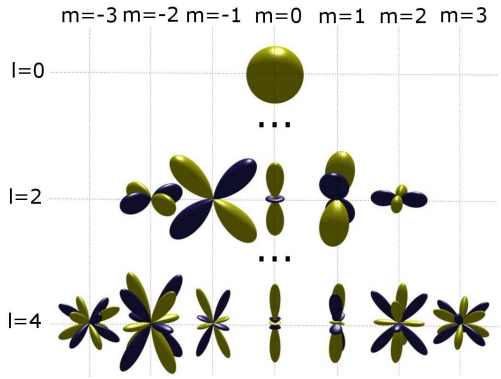

Figure 2: Examples of the spherical harmonics utilized in this work, where Y_1^m and Y_3^m have been omitted for clarity. The magnitude of the spherical harmonic is shown as distance from the origin with positive values yellow and negative values blue. The Y_4^{-3} and Y_4^3 harmonics are sensitive to lattice rotations, while the harmonics with degree m=0 characterize uniaxial compression.

a complete set of orthonormal functions, however here we make use of the first 25, projecting the 2-D PASF onto only these, see Fig. 2.

$$c_l^m = \int_\Omega S(\theta,\phi) Y_l^m(\theta,\phi) d\Omega \tag{2}$$

resulting in a series of coefficients, c_l^m, which can be used to characterize the lattice and discriminate between various deformations. Here, $S(\theta,\phi)$ is the 2-D PASF and $Y_l^m(\theta,\phi)$ the spherical harmonic with order l and degree m.

Table 1: Values of the projected spherical harmonics for the prototypical crystal deformation given in Fig. 1. Values are given for a standard bcc lattice, 20% uniaxial compression along z, a lattice rotation consistent with the {112}<111> twin system in a bcc material and phase transformation to a hcp structure. The value of each coefficient is given to 2 significant figures.

	bcc	bcc_{uc}	bcc_{rot}	hcp
c_0^0	10.4	6.5	10.2	4.7
c_2^0	0.0	-2.8	0.0	-0.8
c_4^{-3}	0.0	0.0	-3.1	0.0
c_4^0	-4.0	3.0	2.6	-1.5
c_4^3	0.0	0.0	3.1	0.0
c_4^4	-3.4	-8.1	-0.1	-0.2

Due to the symmetrical nature of both the spherical harmonics and of reciprocal space, the resultant coefficients are close to zero for most perfect crystals and identically zero for odd order harmonics. As deformation and symmetry breaking occurs, however, they can gain large finite values. Table 1 gives the values of these coefficients calculated for an atom at the centre of a lattice undergoing the idealized deformation cases shown in Fig. 1. While not all coefficients demonstrate large sensitivity to crystal changes it can be see that c_4^{-3} and c_4^3 are particularly sensitive to lattice rotations around x and y, while the coefficients with degree 0 help to characterize uniaxial compression along the z axis, typically aligned along the shock direction. Inspecting the spherical harmonics in Fig. 2 demonstrates that this is due to the negative or low equatorial values and increasingly positive or large values towards the polar regions.

The set of spherical harmonic coefficients can then be used to either visualize or classify the MD simulation on a per-atom basis. This results in a clear identification of each region of the crystal and of the different deformation mechanisms present.

3. Examples

In order to demonstrate the flexibility of the method we investigate two trial systems that represent challenging deformation mechanisms to identify and visualize with current standard techniques. The first is deformation twinning in Ta where the crystal structure remains constant but the lattice undergoes a rotation during deformation-induced twinning. The second is the α to ω phase transformation in Ti which cannot currently be identified with standard real space techniques. All simulations were performed in the LAMMPS code[24] and visualized using the OVITO visualization and analysis software for atomistic simulation data[25].

3.1. Deformation Twinning in Tantalum

We present large scale MD simulations of shock compressed Ta using the extended Finnis-Sinclair potential[26, 27, 28]. As shown previously, for shock waves propagating along the [001] direction at pressures above the Hugoniot elastic limit, stress relaxation occurs through deformation twinning[18, 29]. Although previously studied, here Ta acts as an example where current visualization techniques either fail or require significant input to differentiate between each of the four {112}<111> twin regions. Previous work has utilized

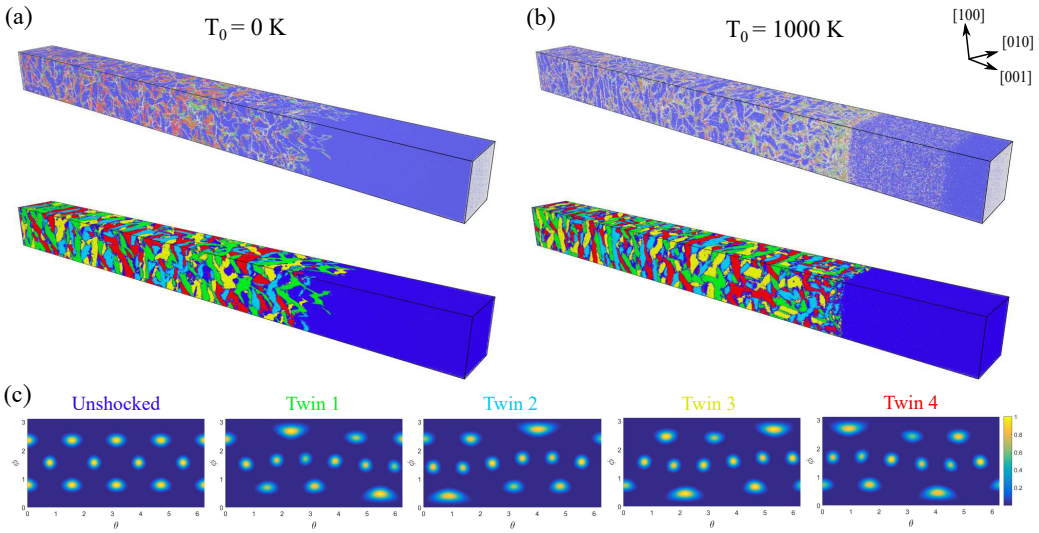

Figure 3: The results of an MD simulation of Ta with a piston velocity of 0.8 km s^{-1} using the extended Finnis-Sinclair potential with an initial temperature of (a) 5 K and (b) 1000 K. The shown sample is $462 \times 462 \times 6605$ $Å^3$ and contains approximately 70 million atoms. The top visualization is colored according to standard CNA techniques (bcc - blue, hcp - red, Uncategorized - white) while the bottom figure shows the results of categorization based upon the spherical harmonics Y_4^{-3} and Y_4^3 detailed in the text. Blue represents the un-twinned orientation with green, red, cyan, and yellow denoting the twinned orientations. Equirectangular projections of the ellipsoid surface for the un-twinned and four twinning categories are shown in (c).

the concept of the PASF represented through planar sections of reciprocal space to identify the four different twin states, however *a*-priori knowledge of the twin systems was required. While this requirement was justified in the case of deformation twining, which obeys specific orientation relationships between parent and twinned crystals, this is not necessarily the case for all structural transformations.

The utilized extended Finnis-Sinclair potential does well to reproduce the zero pressure phonon dispersion curves and the high pressure elastic constants, as well as having excellent agreement between the experimental and simulated shock Hugoniot. Samples of $140 \times 140 \times 2000$ cells ($462 \times 462 \times 6605$ Å^3) were initially thermalized to 5 K and 1000 K before being driven by a reflective wall piston along the [001] direction with a fixed velocity of $U_p = 0.8$ km s^{-1}, generating pressures in excess of the single crystal HEL for this potential ($\sim$50 GPa[18]). It should be noted that this value is far in excess of the HEL of both polycrystalline[30] and single crystal[31] Ta. Thus, it should be used as an opportunity to discuss deformation twinning mechanisms and demonstrate the technique rather than for use as a predictive tool. Periodic boundary conditions were chosen for the two transverse directions. The low starting temperature of 5 K ensures twinning remains the dominant deformation mechanism while the 1000 K simulation is used to demonstrate the robustness of the method at high temperatures.

Adaptive common neighbor analysis[17] was performed with the visualization tool OVITO[25] and is shown in the top image of Fig. 3a. Due to the sensitivity of the coefficients c_4^{-3} and c_4^3 to lattice rotations we utilized these to identify each of the four degenerate {112}<111> twin systems[32] that exist in Ta. Each of the twins are characterized by the value of the coefficients being either both positive, both negative, positive and negative or negative and positive. Values where the modulus of the coefficient was found to be less than 0.5 were left uncategorized. The resultant coloring shown at the bottom of Fig. 3 is similar to previous work but only required knowledge of the equilibrium lattice constant. The common neighbor analysis identifies the appearance of crystallites with the same crystallographic structure as present ahead of the shock, however each of the four twin systems cannot be uniquely identified. For the high temperature case shown in Fig. 3b the CNA analysis performs even more poorly, particularly in the elastically deformed region ahead of the shock. We attribute this to the effect of temperature and lattice vibrations on the real space analysis, while the 2-D PASF technique still adequately identifies each twinned region. A representative atom within

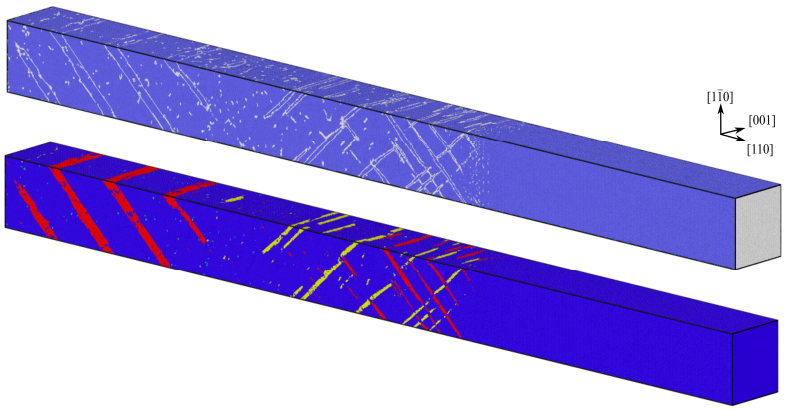

Figure 4: The results of an MD simulation of Ta with a piston velocity of 0.6 km s^{-1} employing a 5 ps ramp. The simulation utilized the Ravelo potential with an initial temperature of 300 K. The shown sample is $231 \times 233 \times 3400$ Å^3 and contains 11,207,000 atoms. The top visualization is colored according to standard CNA techniques (bcc - blue, hcp - red, Uncategorized - white) while the bottom figure shows the results of categorization based upon the spherical harmonics Y_4^{-3} and Y_4^3 detailed in the text. Blue represents the un-twinned orientation with green, red, cyan, and yellow denoting the twinned orientations.

each of the twinned regions was chosen and Fig. 3c shows the equirectangular projection for the original lattice and each of the four twin states. The similarity to the rotated lattice shown in Fig. 1 shows that these are rotated bcc lattices with an orientation relationship in agreement with {112}<111>.

Quantitative information on the state of the system can also be extracted from the simulations. For example, twin volume fraction can be computed by combining the classification of twins with the volume of the particle's Voronoi cell calculated through OVITO[25]. The resultant twin volume fractions are given in Table 2 and are consistent with previous high volume fractions found for the Finnis-Sinclair potential [18]. We also demonstrate our method with a potential that predicts a substantially lower twinning fraction by utilizing the Ta1 potential created by Ravelo *et* al.[29]. A Ti crystal $231 \times 233 \times 3400$ Å^3 in volume and consisting of ∼11 million atoms was thermalised to 300 K. Following the procedure detailed in [29] the crystal is shocked along the [110] direction with a piston velocity of 0.6 km s^{-1} initiated with a 5 ps ramp. A snapshot of the simulation taken at 60 ps was analyzed with the SH method and the CNA technique, see Fig. 4. In agreement with previous work we find twin nucleation at the shock front and twins that rapidly thicken and

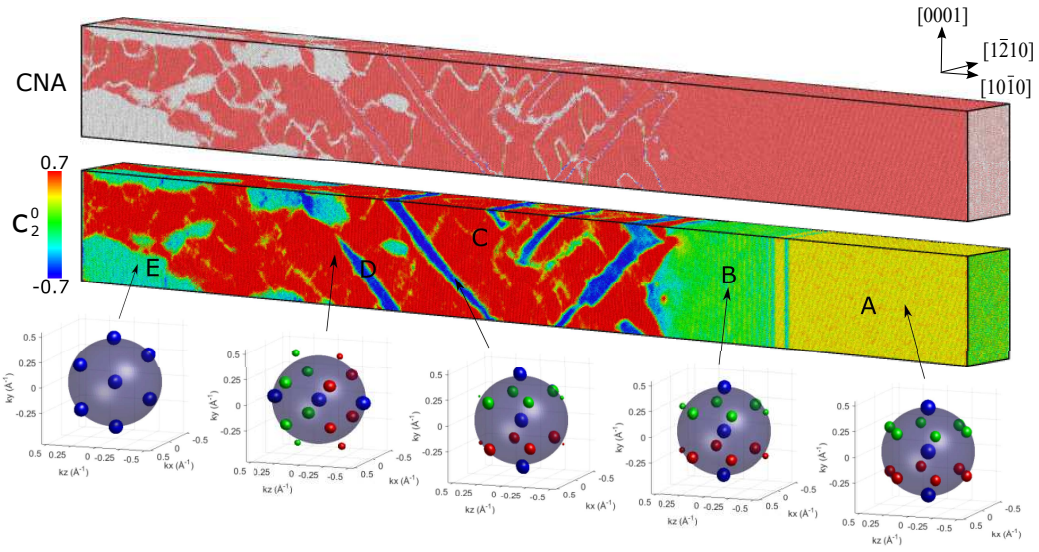

Figure 5: The results of an MD simulation of Ti with a piston velocity of 0.75 km s^{-1} using the Trinkle potential with an initial temperature of 30 K. The shown sample is $147 \times 234 \times 2556$ Å^3 and contains 5012500 atoms. The top visualization is coloured according to standard CNA techniques (bcc - blue, hcp - red, Uncategorised - white) while the bottom figure shows the coefficient of the Y_2^0 spherical harmonic. Each region (unshocked, uniaxially compressed, 90° lattice rotation, phase transformation to ω) is clearly visible while the full 3-D PASF allows phase identification.

grow. However, in contrast to the Finnis-Sinclair potential, only two twin orientations are present and a significantly lower twin volume fraction of 10.6% is found. This calculated twin volume fraction is more similar to that found in nano-indentation experiments on Ta[33].

Table 2: Values of the twin volume fraction in shock compressed Ta using the extended Finnis-Sinclair (FS) potential and the Ravelo potential. The twin volume was calculated by combining the classification mechanism defined in the text with the volume of each particle's Voronoi cell.

Twin Variant	FS_{0K}	FS_{1000K}	$Ravelo_{300K}$
1	18.7%	19.2%	0.1%
2	24.9%	21.3%	0.1%
3	17.9%	19.9%	3.6%
4	22.0%	20.7%	7.0%
Total	83.5%	81.1%	10.6%

3.2. Twinning and Phase change in Titanium

Secondly we present large scale MD simulations of shock compressed Ti. Ti is a group-IV hcp metal which undergoes an α (hcp) to ω (hexagonal) phase transition at high pressure. This phase transition has been extensively studied both computationally and experimentally and, when using the Trinkle potential[34, 35], the phase transition proceeds through a collective deformation mode, namely a 90° lattice rotation that does not conform to any known hcp twin systems. Furthermore, the ω phase can be difficult to identify with standard techniques such as common neighbour analysis. Here we show that the c_2^0 spherical harmonic coefficient is able to identify the elastic compression, lattice rotation and phase transition in a single parameter and that the 3-D PASF allows easy identification in each region.

Simulations of $50 \times 50 \times 500$ cells ($147 \times 234 \times 2556$ Å^3) containing 5012500 atoms were initially thermalized to 30 K before being driven by a reflective wall piston along the $[10\bar{1}0]$ direction with a fixed velocity of $U_p = 0.75$ km s^{-1}. Periodic boundary conditions were chosen for the two transverse directions. The top image in Fig. 5 has been colored according to adaptive common neighbor analysis while the bottom figure is coloured according to the c_2^0 spherical harmonic coefficient. Five distinct regions are clearly identified. A representative atom in the centre of each region was

selected and the 3-D PASF is shown. The initial un-shocked sample (region A) has the characteristic PASF for a hcp lattice, a hexagonal pattern interspersed with a central line of points. Initially the sample undergoes uniaxial compression along the shock direction; this compression in real space manifests as an expansion in reciprocal space, the spots highlighted by the isosurface move outwards (region B). Secondly the 90° lattice rotation occurs from region B to C, resulting in a 90° reflection of the PASF about the k_x axis, although regions of un-rotated sample at a higher compression remain (region D). The final deformation mechanism is a phase change from α to ω. The ω phase is identifiable by a central point surrounded by a hexagon of neighboring k-space points, while for the hcp lattice the central point is offset. The phase transition here is consistent with the orientation relationship found in previous work[36, 37]. Each region is clearly identified by the c_2^0 spherical harmonic coefficient.

4. Conclusion

An extension of a technique for identification of both elastic and plastic deformation in molecular dynamics simulations is presented. In agreement with previous work, the full 3-D per atom structure factor, although computationally intensive, is shown to easily identify elastic deformation, twinning and phase changes, even at high temperatures and with the large defect concentrations present in high-rate deformation. A faster and less computationally intensive method based around taking a 2-D ellipsoid slice of reciprocal space was shown to retain a significant portion of the information contained in the 3-D counterpart and furthermore could be projected onto the set of spherical harmonics to provide a numerical value for classification or visualization.

The method was demonstrated on two test cases. In shock compressed Ta each of the four {112}<111> twin systems were able to be visualized using the spherical harmonics Y_1^{-1} and Y_1^1. In shock compressed Ti the same method but utilizing the Y_2^0 spherical harmonic was successfully able to simultaneously visualize deformation regions corresponding to uniaxial elastic compression, lattice rotation and the α to ω phase transition.

The robustness and speed of this method suggest that building both the 2-D PASF and 3-D PASF into existing MD visualization software or post-processing tools would be beneficial to those studying shock deformation. Future work involving modifying the ellipsoid dynamically would improve

generality of the model. Furthermore, the reduction of information from the 3-D PASF, to the 2-D PASF and finally the set of spherical harmonic coefficients could one day be used together with machine learning algorithms to aid in identification of lattice deformation mechanics.

[1] A. Higginbotham, P. G. Stubley, A. J. Comley, J. H. Eggert, J. M. Foster, D. H. Kalantar, D. McGonegle, S. Patel, L. J. Peacock, S. D. Rothman, R. F. Smith, M. J. Suggit and J. S. Wark, Sci. Rep. **6**, 24211 (2016).

[2] B. L. Holian, Shock Waves **13**, 489 (2004).

[3] M. A. Morales, E. Schwegler, D. Ceperley, C. Pierleoni, S. Hamel and K. Caspersen, PNAS **106(5)**, 13241329 (2009).

[4] N Pineau, J. Phys. Chem. C **117(24)**, 12778 (2013).

[5] O. A. Hurricane, D. A. Callahan, D. T. Casey, P. M. Celliers, C. Cerjan, E. L. Dewald, T. R. Dittrich, T. Döppner, D. E. Hinkel, L. F. Berzak Hopkins, J. L. Kline, S. Le Pape, T. Ma, A. G. MacPhee, J. L. Milovich, A. Pak, H.-S. Park, P. K. Patel, B. A. Remington, J. D. Salmonson, P. T. Springer and R. Tommasini, Nature **506**, 343348 (2014).

[6] L. B. Fletcher, H. J. Lee, T. Döppner, E. Galtier, B. Nagler, P. Heimann, C. Fortmann, S. LePape, T. Ma, M. Millot, A. Pak, D. Turnbull, D. A. Chapman, D. O. Gericke, J. Vorberger, T. White, G. Gregori, M. Wei, B. Barbrel, R. W. Falcone, C.-C. Kao, H. Nuhn, J. Welch, U. Zastrau, P. Neumayer, J. B. Hastings and S. H. Glenzer, Nat. Photonics **9 (4)**, 274-279 (2015).

[7] J. M. McNaney, M. J. Edwards, R. Becker, K. T. Lorenz, and B. A. Remington, Mettal. Trans. A **35A**, 26252631 (2004).

[8] B. A. Remington *et al.*, Mettal. Trans. A **35A**, 25872608 (2004).

[9] E. M. Bringa, K. Rosolankova, R. E. Rudd, B. A. Remington, J. S. Wark, M. Duchaineau, D. H. Kalantar, J. Hawreliak and J. Belak, Nat. Mater. **5**, 805 - 809 (2006).

[10] V. Dupont and T. C. Germann, Phys. Rev. B **86**, 134111 (2012).

[11] D. Milathianaki, S. Boutet, G. J. Williams, A. Higginbotham, D. Ratner, A. E. Gleason, M. Messerschmidt, M. M. Seibert, D. C. Swift, P. Hering, J. Robinson, W. E. White, J. S. Wark, Science **342**, 220 (2013).

[12] T. D. Swinburne, M. G. Glavicic, K. M. Rahman, N. G. Jones, J. Coakley, D. E. Eakins, T. G. White, V. Tong, D. Milathianaki, G. J. Williams, D. Rugg, A. P. Sutton, and D. Dye, Phys. Rev. B **93 (14)**, 144119 (2016).

[13] T. G. White, P. Mabey, D. O. Gericke, N. J. Hartley, H. W. Doyle, D. McGonegle, D. S. Rackstraw, A. Higginbotham, and G. Gregori, Phys. Rev. B **90**, 014305 (2014).

[14] J. D. Honeycutt and H. C. Andersen, J. Phys. Chem. **91(19)**, 49504963 (1987).

[15] Cynthia L. Kelchner, S. J. Plimpton, and J. C. Hamilton, Phys. Rev. B **58(17)**, 11085 (1998).

[16] G. J. Ackland and A. P. Jones, Phys. Rev. B **73(5)**, 054104 (2006).

[17] A. Stukowski, Modell. Simul. Mater. Sci. Eng. **20**, 045021 (2012).

[18] A. Higginbotham, M. J. Suggit, E. M. Bringa, P. Erhart, J. A. Hawreliak, G. Mogni, N. Park, B. A. Remington, and J. S. Wark, Phys. Rev. B **88**, 104105 (2013).

[19] P. J. Steinhardt, D. R. Nelson and M. Ronchetti, Phys. Rev. B **28**, 784 (1983).

[20] P. R. ten Wolde, M. J. Ruiz-Montero, and D. Frenkel, J. Chem. Phys. **104**, 9932 (1996).

[21] W. Lechner and C. Dellago, J. Chem. Phys. **129**, 114707 (2008).

[22] A. S. Keys, C. R. Iacovella and S. C. Glotzer, J. Comp. Phys. **230** 6438 (2011).

[23] B. E. Warren, *X-ray diffraction* (Addison-Wesley, Reading, 1969).

[24] S. Plimpton, J. Comput. Phys. **117**, 1 (1995).

[25] A. Stukowski, Modelling Simul. Mater. Sci. Eng.**18**, 015012 (2010).

[26] X. D. Dai, Y. Kong, J. H. Li, and B. X. Liu, J. Phys.: Condens. Matter **18**, 4527 (2006).

[27] M. S. Daw and M. I Baskes, Phys. Rev. Lett. **50**, 1285 (1983).

[28] M. W. Finnis and J. E. Sinclair, Phil. Mag. A **50**, 45 (1984).

[29] R. Ravelo, T. C. Germann, O. Guerrero, Q. An, and B. L. Holian, Phys. Rev. B **88**, 134101 (2013).

[30] S. V. Razorenov, G. Garkushin, G. I. Kanel and O. N. Ignatova, AIP Conf. Proc. **1426**, 991 (2012).

[31] G. Whiteman, S. Case and J C F Millett, J. Phys.: Conference Series **500**, 112067 (2014).

[32] J. W. Christian and S. Mahajan, Prog. Mater. Sci. **39**, 1 (1995).

[33] R. J. McCabe, I. J. Beyerlein, J. S. Carpenter and N. A. Mara, Nat. Coms. **5**, 3806 (2014).

[34] R. G. Hennig, T. J. Lenosky, D. R. Trinkle, S. P. Rudin, and J. W. Wilkins, Phys. Rev. B **78**, 054121 (2008).

[35] D. R. Trinkle, Ph.D. thesis, The Ohio State University, Columbus, 2003.

[36] H. Zong, X. Ding, T. Lookman, J. Li, J. Sun, E. K. Cerreta, J. P. Escobedo, F. L. Addessio, and C. A. Bronkhorst, Phys. Rev. B **89**, 220101 (2014).

[37] D. McGonegle, D. Milathianaki, B. A. Remington, J. S. Wark and A. Higginbotham, J. Appl. Phys. **118**, 065902 (2015).